















Debris Disk Color with the *Hubble Space Telescope*

Bin B. Ren (任彬) ^{1,2,3}, Isabel Rebullido ⁴, Élodie Choquet ⁵, Wen-Han Zhou (周文翰) ¹, Marshall D. Perrin ⁴, Glenn Schneider ⁶, Julien Milli ², Schuyler G. Wolff ⁶, Christine H. Chen ⁴, John H. Debes ⁴, J. Brendan Hagan⁴, Dean C. Hines ⁴, Maxwell A. Millar-Blanchaer ⁸, Laurent Pueyo⁴, Aki Roberge ⁹, Eugene Serabyn⁷, and Rémi Soumer ⁴

¹ Université Côte d’Azur, Observatoire de la Côte d’Azur, CNRS, Laboratoire Lagrange, F-06304 Nice, France; e-mail: bin.ren@oca.eu

² Université Grenoble Alpes, CNRS, Institut de Planétologie et d’Astrophysique (IPAG), F-38000 Grenoble, France

³ Department of Astronomy, California Institute of Technology, MC 249-17, 1200 East California Boulevard, Pasadena, CA 91125, USA

⁴ Space Telescope Science Institute (STScI), 3700 San Martin Drive, Baltimore, MD 21218, USA

⁵ Aix Marseille Univ, CNRS, CNES, LAM, Marseille, France

⁶ Steward Observatory, The University of Arizona, Tucson, AZ 85721, USA

⁷ Jet Propulsion Laboratory, California Institute of Technology, 4800 Oak Grove Drive, Pasadena, CA 91109, USA

⁸ Department of Physics, University of California, Santa Barbara, CA 93106, USA

⁹ Astrophysics Science Division, NASA Goddard Space Flight Center, Greenbelt, MD 20771, USA

Received 14 November 2022; revised 7 February 2023; accepted 8 February 2023

ABSTRACT

Context. Multi-wavelength scattered light imaging of debris disks may inform dust properties including typical size and mineral composition. Existing studies have investigated a small set of individual systems across a variety of imaging instruments and filters, calling for uniform comparison studies to systematically investigate dust properties.

Aims. We obtain the surface brightness of dust particles in debris disks by post-processing coronagraphic imaging observations, and compare the multi-wavelength reflectance of dust. For a sample of resolved debris disks, we perform a systematic analysis on the reflectance properties of their birth rings.

Methods. We reduced the visible and near-infrared images of 23 debris disk systems hosted by A through M stars using two coronagraphs onboard the *Hubble Space Telescope*: the STIS instrument observations centering at 0.58 μm , and the NICMOS instrument at 1.12 μm or 1.60 μm . For proper recovery of debris disks, we used classical reference differential imaging for STIS, and adopted non-negative matrix factorization with forward modeling for NICMOS. By dividing disk signals by stellar signals to take into account of intrinsic stellar color effects, we systematically obtained and compared the reflectance of debris birth rings at $\approx 90^\circ$ scattering angle.

Results. Debris birth rings typically exhibit a blue color at $\approx 90^\circ$ scattering angle. As the stellar luminosity increases, the color tends to be more neutral. A likely L-shaped color-albedo distribution indicates a clustering of scatterer properties.

Conclusions. The observed color trend correlates with the expected blow-out size of dust particles. The color–albedo clustering likely suggests different populations of dust in these systems. More detailed radiative transfer models with realistic dust morphology will contribute to explaining the observed color and color-albedo distribution of debris systems.

Key words. stars: imaging – instrumentation: high angular resolution – techniques: image processing – Kuiper Belt: general

1. Introduction

Debris disks are extrasolar analogs of the Asteroid Belt and the Kuiper Belt (e.g. Hughes et al. 2018). They are composed of second-generation dust, in the sense that their life time is shorter than the age of their host star (e.g., Wyatt 2008), and they are produced from and continuously replenished by collisional cascade of larger solid bodies (Dohnanyi 1969). While collisional cascade produces small dust particles, radiation pressure can surpass gravity for small dust particles and blow certain dust particles out of stellar systems (e.g., Strubbe & Chiang 2006; Krivov et al. 2006). The balance of forces for dust particles results in a blow-out size, which ranges from sub-micron to several microns depending on both stellar properties and dust properties (e.g., spectral type, dust composition, dust porosity: Arnold et al. 2019). Observationally, depending on the blow-out size and

other dust properties in disks, there could exist noticeable differences (e.g., scattering phase function: Muñoz et al. 2021).

In the birth ring of a debris disk, dust particles under collisional cascade have an expected number distribution $n(a) \propto a^{-3.5}$ where a is the particle size (e.g., Pan & Schlichting 2012). Under the fact that the cross section of each particle is proportional to a^2 , collisional cascade can make the smaller particles dominate more surface area of a debris disk. In reality, stellar radiation pressure can drive smaller particles to higher-eccentricity or even unbound orbits, resulting into blow-out sizes above which dust particles are bound. Nevertheless, the balance between radiation and gravity predicts that dust particles can be unbound only within a certain size range (e.g., Thebault & Kral 2019), and that there is no stellar-radiation-driven blow-out size for certain later-type stars (e.g., M stars: Arnold et al. 2019). Other mechanisms, including stellar winds in M stars (e.g., AU Mic: Augereau &

Beust 2006, TWA 7: Olofsson et al. 2020), can also remove dust particles from stellar environments, complicating the size distribution of dust in debris systems. The joint effect of these mechanisms could lead to observational complexity for debris disks.

Studies on spectral energy distribution (SED) of debris disks showed that the ratio between dust temperature and blackbody temperature at the disk radius decreases with increasing stellar luminosity (e.g. Pawellek et al. 2014). Although this trend can be explained by the hypothesis that typical dust size increases with stellar luminosity (Pawellek et al. 2014; Pawellek & Krivov 2015), the blackbody location of disks can offset from their resolved locations by a factor of ~ 4 (e.g., scattered light imaging: Esposito et al. 2020), since debris dust particles are inefficient emitters at longer wavelengths. This offset makes SED modeling a degenerate problem between dust property and disk location. With resolved disk images in scattered light, we can break these known degeneracies for the smallest dust in debris systems.

Using a variety of coronagraphic imaging instruments from both the ground (e.g., NaCo: Lagrange et al. 2003; Lenzen et al. 2003, GPI: Macintosh et al. 2008, SPHERE: Beuzit et al. 2008) and the space (e.g., ACS: Ford et al. 1998, NICMOS: Ramberg 1993, STIS: Woodgate et al. 1998), multi-wavelength scattered light imaging studies revealed dust properties for debris disks individually, such as 49 Ceti (Choquet et al. 2017; Pawellek et al. 2019), AU Mic (Fitzgerald et al. 2007), Beta Pic (Golimowski et al. 2006), HD 15115 (Kalas et al. 2007), HD 32297 (Kalas 2005; Duchêne et al. 2020), HD 35841 (Esposito et al. 2018), HD 107146 (Ertel et al. 2011), HD 191089 (Ren et al. 2019), HD 192758 (Choquet et al. 2018), HR 4796A (Debes et al. 2008; Milli et al. 2015; Rodigas et al. 2015; Chen et al. 2020; Arriaga et al. 2020), and TWA 7 (Ren et al. 2021). These multi-wavelength studies, when further augmented with the advantage of uniform imaging exploration from identical instruments (e.g., GPI debris disk survey: Esposito et al. 2020), would minimize the offsets from different instruments to enable uniform systematic studies of dust properties, thus bring forth essential information on the ensemble properties of debris disks in scattered light.

With debris disks resolved in scattered light, existing studies have investigated their ensemble properties, especially on scattering phase functions (SPFs) which depict the scattered light intensity dependence on scattering angles. Hughes et al. (2018) suggested that the SPFs of debris disks could follow a uniform trend, yet more recent observations with high-precision measurements showed diverse SPFs in different systems (e.g., Ren et al. 2019; Engler et al. 2022) or even potential SPF change in different wavelengths (e.g., Ren et al. 2020). In addition, SPF measurements could be impacted by instrumentation effects including convolution, by data reduction artifacts such as over-fitting and self-subtraction in high-contrast total intensity imaging, and by vertical thickness effects (e.g., Milli et al. 2017; Olofsson et al. 2020), these complications make it a necessity to study debris disks from another complementary perspective – multi-band imaging (e.g., Chen et al. 2020; Arriaga et al. 2020) – to depict their collective properties.

Onboard the *Hubble Space Telescope* (*HST*), the Space Telescope Imaging Spectrograph (STIS: Woodgate et al. 1998) and Near Infrared Camera and Multi-Object Spectrometer (NICMOS: Thompson 1992) instruments can offer unparalleled stability and sensitivity in the coronagraphic imaging of circumstellar disks from visible light to near infrared wavelengths. In comparison with protoplanetary disks that are relatively bright and facile to be attempted from ground-based extreme-adaptive-optics-equipped systems in polarized light (e.g., Avenhaus et al.

2018; Laws et al. 2020), *HST* coronagraphs can offer both stable stellar point spread function (PSF) and optimal sensitivity for faint target imaging. These advanced instruments provide the most effective method for imaging faint debris disks in total intensity (e.g., STIS: Krist et al. 2010, 2012; Schneider et al. 2018). In addition, the fact that *HST* operates in vacuum makes it not only straightforward to calibrate detector readouts to physical units (e.g., Viana et al. 2009) than ground-based observations (e.g., Milli et al. 2015), but also sensitive to the faintest materials such as debris halos that are elusive from the ground (e.g., halos: Schneider et al. 2018; Ren et al. 2019).

With the high-stability, high-sensitivity, and high-spatial-resolution offered by *HST*, resolved scattered light imaging of debris disks can directly probe the spatial and surface brightness distributions for the smallest dust particles within (e.g., Schneider et al. 2014, 2018). When imaged at multiple wavelengths, the color information of the scatterers can inform dust properties (e.g., composition, porosity: Debes et al. 2008). In addition, resolved imaging of debris disks enabled by application of advanced statistical methods, especially when applied to archival observations and recovering the hidden debris disks (e.g., Soummer et al. 2014; Choquet et al. 2014), can allow the study of dust properties to an unprecedented degree (e.g., albedo: Choquet et al. 2018). Combining the advantages of multi-wavelength images offered by *HST* and disk recovery from advanced methods, here we perform a uniform recovery and study of resolved debris disks to investigate their ensemble properties. We describe the observation and the data reduction procedures to recover resolved disk images in Sect. 2, analyze the data in Sect. 3, discuss our findings in Sect. 4, and conclude this study in Sect. 4.

2. Observation & Data Reduction

We summarized a total of 23 systems observed in coronagraphic imaging mode using both STIS (filter: 50CORON; $\lambda_c = 0.58 \mu\text{m}$, pixel scale: $50.72 \text{ mas pixel}^{-1}$, Riley et al. 2018) and NICMOS Camera 2 (NIC2; filter: F110W or F160W; $\lambda_c = 1.12 \mu\text{m}$ or $1.60 \mu\text{m}$, pixel scale: $75.65 \text{ mas pixel}^{-1}$, Viana et al. 2009). In Fig. 1, we display the transmission curves of the three filters (obtained from Rodrigo et al. 2012; Rodrigo & Solano 2020). The debris systems are: 49 Ceti, AU Mic, Beta Pic, HD 377, HD 15115, HD 15745, HD 30447, HD 32297, HD 35650, HD 35841, HD 61005, HD 104860, HD 110058, HD 131835, HD 141569A, HD 141943, HD 181327, HD 191089, HD 192758, HD 202917, HR 4796A, TWA 7, and TWA 25. We summarize the properties¹ of the targets in Table 1, and the exposure information in Table A.1.

2.1. STIS

Using STIS, we observed 4 systems (HD 30447, HD 35841, HD 141943, and HD 191089) under *HST* GO-13381² (PI: M. Perrin), 9 systems (49 Ceti, HD 377, HD 35650, HD 104860, HD 110058, HD 131835, HD 192758, TWA 7, and TWA 25) under *HST* GO-15218³ (PI: É. Choquet). From the MAST archive,⁴

¹ Unless otherwise specified, the error bars calculated in this paper are 1σ .

² <https://www.stsci.edu/cgi-bin/get-proposal-info?id=13381&observatory=HST>

³ <https://www.stsci.edu/cgi-bin/get-proposal-info?id=15218&observatory=HST>

⁴ <https://archive.stsci.edu>

Table 1. Property of debris disk hosts observed by *HST*/STIS and *HST*/NICMOS

id	Target	SpType	V (mag)	Distance (pc)	T_{eff} (K)	M_{star} (M_{\odot})	L_{star} (L_{\odot})	$\log g$ (cm s^{-2})	a_{BO} (μm)	Reference SpType	V -mag
(1)	(2)	(3)	(4)	(5)	(6)	(7)	(8)	(9)	(10)	(11)	(12)
<i>a</i>	49 Ceti	A1V	5.61	57.23 ^{+0.18} _{-0.18}	9000 ⁺¹⁷⁰ ₋₄₀₀	2.2 ^{+0.3} _{-0.3}	15.7 ^{+0.7} _{-0.7}	4.32 ^{+0.07} _{-0.07}	2.5 ^{+0.4} _{-0.4}	1	13
<i>b</i>	AU Mic	M1V	8.63	9.714 ^{+0.002} _{-0.002}	3992 ⁺¹⁵⁰ ₋₁₆₆	0.710 ^{+0.014} _{-0.014}	0.073 ^{+0.004} _{-0.004}	4.6 ^{+0.06} _{-0.06}	0.036 ^{+0.002} _{-0.002}	2	14
<i>c</i>	Beta Pic	A6V	3.86	19.63 ^{+0.06} _{-0.06}	7100 ⁺³⁰⁰ ₋₃₀₀	1.9 ^{+0.2} _{-0.2}	8.97 ^{+0.07} _{-0.07}	4.4 ^{+0.3} _{-0.3}	1.65 ^{+0.17} _{-0.17}	3	15
<i>d</i>	HD 377	G2V	7.59	38.40 ^{+0.04} _{-0.04}	5871 ⁺³⁰ ₋₄₀	1.07 ^{+0.13} _{-0.13}	1.16 ^{+0.03} _{-0.03}	4.44 ^{+0.08} _{-0.08}	0.38 ^{+0.15} _{-0.15}	4	15
<i>e</i>	HD 15115	F4IV	6.80	48.77 ^{+0.07} _{-0.07}	6811 ⁺¹⁵⁰ ₋₁₅₀	1.4 ^{+0.2} _{-0.2}	3.73 ^{+0.13} _{-0.13}	4.31 ^{+0.08} _{-0.08}	0.90 ^{+0.15} _{-0.15}	5	16
<i>f</i>	HD 15745	F0	7.49	71.73 ^{+0.12} _{-0.12}	6840 ⁺¹⁵⁰ ₋₁₅₀	1.5 ^{+0.3} _{-0.3}	4.21 ^{+0.17} _{-0.17}	4.27 ^{+0.08} _{-0.08}	1.0 ^{+0.18} _{-0.18}	6	16
<i>g</i>	HD 30447	F3V	7.86	80.31 ^{+0.14} _{-0.14}	6709 ⁺¹⁴⁰ ₋₁₄₀	1.5 ^{+0.3} _{-0.3}	3.73 ^{+0.14} _{-0.14}	4.31 ^{+0.09} _{-0.09}	0.89 ^{+0.16} _{-0.16}	7	16
<i>h</i>	HD 32297	A6V	8.14	129.7 ^{+0.5} _{-0.5}	7980 ⁺⁸⁰ ₋₈₀	1.9 ^{+0.3} _{-0.3}	8.5 ^{+0.4} _{-0.4}	4.36 ^{+0.08} _{-0.08}	1.5 ^{+0.3} _{-0.3}	8	16
<i>i</i>	HD 35650	K6V	9.05	17.461 ^{+0.005} _{-0.005}	4175 ⁺¹⁵⁰ ₋₆₀	0.66 ^{+0.08} _{-0.08}	0.129 ^{+0.009} _{-0.009}	4.6 ^{+0.11} _{-0.11}	0.069 ^{+0.010} _{-0.010}	4	17
<i>j</i>	HD 35841	F3V	8.90	103.07 ^{+0.14} _{-0.14}	6305 ⁺²⁰⁰ ₋₈₀	1.3 ^{+0.2} _{-0.2}	2.43 ^{+0.10} _{-0.10}	4.38 ^{+0.09} _{-0.09}	0.64 ^{+0.11} _{-0.11}	1	16
<i>k</i>	HD 61005	G8V	8.22	36.45 ^{+0.02} _{-0.02}	5507 ⁺⁶⁰ ₋₁₂₀	0.97 ^{+0.12} _{-0.12}	0.636 ^{+0.014} _{-0.014}	4.54 ^{+0.07} _{-0.07}	0.23 ^{+0.03} _{-0.03}	3	16
<i>l</i>	HD 104860	G0/F9V	7.91	45.19 ^{+0.04} _{-0.04}	5939 ⁺⁶⁰ ₋₁₀₀	1.11 ^{+0.15} _{-0.15}	1.18 ^{+0.04} _{-0.04}	4.48 ^{+0.08} _{-0.08}	0.37 ^{+0.05} _{-0.05}	9	16
<i>m</i>	HD 110058	A0V	7.97	130.1 ^{+0.5} _{-0.5}	8039 ⁺⁹⁰⁰ ₋₁₉₀	2.0 ^{+0.3} _{-0.3}	9.4 ^{+0.5} _{-0.5}	4.4 ^{+0.08} _{-0.08}	1.6 ^{+0.3} _{-0.3}	10	16
<i>n</i>	HD 131835	A2IV	7.86	129.7 ^{+0.5} _{-0.5}	8266 ⁺³⁰⁰ ₋₃₀₀	2.1 ^{+0.3} _{-0.3}	10.9 ^{+0.9} _{-0.9}	4.37 ^{+0.08} _{-0.08}	1.8 ^{+0.3} _{-0.3}	7	16
<i>o</i>	HD 141569	A2V	7.12	111.6 ^{+0.4} _{-0.4}	8439 ⁺²⁰⁰ ₋₇₀₀	2.1 ^{+0.4} _{-0.4}	15.3 ^{+4.0} _{-4.0}	4.2 ^{+0.3} _{-0.3}	2.5 ^{+0.8} _{-0.8}	11	16
<i>p</i>	HD 141943	G2	7.97	60.14 ^{+0.08} _{-0.08}	5673 ⁺¹⁰⁰ ₋₁₁₀	1.09 ^{+0.14} _{-0.14}	2.07 ^{+0.06} _{-0.06}	4.22 ^{+0.08} _{-0.08}	0.66 ^{+0.09} _{-0.09}	4	17
<i>q</i>	HD 181327	F6V	7.04	47.78 ^{+0.07} _{-0.07}	6436 ⁺⁴⁰ ₋₁₆₀	1.3 ^{+0.2} _{-0.2}	2.88 ^{+0.11} _{-0.11}	4.3 ^{+0.08} _{-0.08}	0.76 ^{+0.13} _{-0.13}	4	16
<i>r</i>	HD 191089	F5V	7.18	50.11 ^{+0.05} _{-0.05}	6450 ⁺⁵⁰ ₋₁₈₀	1.3 ^{+0.2} _{-0.2}	2.74 ^{+0.10} _{-0.10}	4.33 ^{+0.09} _{-0.09}	0.72 ^{+0.12} _{-0.12}	7	16
<i>s</i>	HD 192758	F0V	7.03	66.50 ^{+0.14} _{-0.14}	7200 ⁺¹⁶⁰ ₋₂₀₀	1.6 ^{+0.3} _{-0.3}	5.4 ^{+0.2} _{-0.2}	4.26 ^{+0.09} _{-0.09}	1.2 ^{+0.2} _{-0.2}	10	19
<i>t</i>	HD 202917	G7V	8.67	46.71 ^{+0.03} _{-0.03}	5506 ⁺⁷⁰ ₋₁₀₀	0.98 ^{+0.12} _{-0.12}	0.668 ^{+0.016} _{-0.016}	4.53 ^{+0.08} _{-0.08}	0.24 ^{+0.03} _{-0.03}	4	19
<i>u</i>	HR 4796A	A0V	5.77	70.8 ^{+0.2} _{-0.2}	9670 ⁺¹⁰⁰ ₋₅₀₀	2.5 ^{+0.3} _{-0.3}	24.7 ^{+1.1} _{-1.1}	4.35 ^{+0.06} _{-0.06}	3.5 ^{+0.5} _{-0.5}	7	16
<i>v</i>	TWA 7	M2V	10.91	34.10 ^{+0.03} _{-0.03}	4018 ⁺¹⁵⁰ ₋₁₇₀	0.46 ^{+0.09} _{-0.09}	0.115 ^{+0.019} _{-0.019}	4.18 ^{+0.17} _{-0.17}	0.09 ^{+0.02} _{-0.02}	4	16
<i>w</i>	TWA 25	M0.5	11.16	53.60 ^{+0.07} _{-0.07}	4020 ⁺²⁰⁰ ₋₁₆₀	0.60 ^{+0.08} _{-0.08}	0.23 ^{+0.02} _{-0.02}	4.17 ^{+0.13} _{-0.13}	0.14 ^{+0.02} _{-0.02}	12	17

Notes: Column (1): letter identifiers of the targets in this paper. Column (2): target name. Column (3): spectral type from the literature (column 11). Column (4): V -band magnitude from literature studies in Column (12). Column (5): distance computed from *Gaia* DR3 parallaxes (*Gaia* Collaboration et al. 2022). Column (6): effective temperature from *Gaia* DR2 (*Gaia* Collaboration et al. 2018). Values in Column (7) for star mass, Column (8) for stellar luminosity, and Column (9) for stellar surface gravity are from the *Transiting Exoplanet Survey Satellite* input catalog (Stassun et al. 2018). Column (10): expected dust blowout size for non-porous amorphous olivine using Equation (5). While M stars do not have sufficient radiation pressure to blow small dust out (e.g., Arnold et al. 2019), we report the corresponding blow-out sizes for color-size correlation analysis in Sect. 4.2.

^aFor Beta Pic, the uncertainties of M_{star} , L_{star} , and $\log g$ are scaled from David & Hillenbrand (2015), Anders et al. (2019), and *Gaia* Collaboration et al. (2018), respectively. If the upper and lower uncertainties are different, the bigger one is adopted.

References: In Column (11) and Column (12), the references are for spectral type and V -mag, respectively: (1) Houk & Smith-Moore (1988); (2) Keenan & McNeil (1989); (3) Gray et al. (2006); (4) Torres et al. (2006); (5) Harlan (1974); (6) Cannon & Pickering (1993); (7) Houk (1982); (8) Rodigas et al. (2014); (9) Kahraman Aliçavuş et al. (2016); (10) Houk (1978); (11) Gray et al. (2017); (12) Herczeg & Hillenbrand (2014); (13) Høg et al. (2000); (14) Kiraga (2012); (15) Ducati (2002); (16) Wenger et al. (2000); (17) Zacharias et al. (2012).

we retrieved 6 systems (AU Mic, HD 15115, HD 15745, HD 32297, HD 61005, and HD 181327) from *HST* GO-12228 (PI: G. Schneider; Schneider et al. 2014), 2 systems (HD 202917 and HR 4796A) from *HST* GO-13786 (PI: G. Schneider; Schneider et al. 2016, 2018). For Beta Pic, we retrieved its observations from three programs: SM2/ERO-7125 (PI: S. Heap; Heap et al. 2000), *HST* GO-12551 (PI: D. Apai; Apai et al. 2015) and *HST* GO-12923 (PI: A. Gaspar; Schneider et al. 2017). For HD 141569A, from three programs: *HST* GO-8624 (PI: A. Weinberger), *HST* GO-8674 (PI: A.-M. Lagrange; Mouillet et al. 2001) and *HST* GO-13786 (PI: G. Schneider; Konishi et al. 2016).

For each target, we reduced the observation data with multi-roll combined PSF-template subtraction (MRDI: Schneider et al. 2014) using its corresponding PSF reference images designated in each *HST* program. We note that although HD 377 was previously observed in *HST* GO-12291 (PI: J. Krist), it was not recovered since the major axis of the disk coincides with either the STIS occulter or the diffraction spikes. In addition, we

observed negligible difference between median-combined and mean-combined images, and thus we used the mean-combined MRDI images for a proper propagation of errors. We present the reduced images in Fig. 2.

2.2. NICMOS

We assembled the NICMOS observations for the targets and their corresponding PSF references from the Archival Legacy Investigations of Circumstellar Environments (ALICE) project⁵ (PI: R. Soummer; Choquet et al. 2014; Hagan et al. 2018). We reduced the data with the non-negative matrix factorization method (NMF: Ren et al. 2018) using 30% of the most correlated references with 50 sequentially constructed NMF components. To recover the true surface brightness of these disks, we adopted a forward modeling approach assuming simple geometric models for debris architecture (Augereau et al. 1999) and analytical SPFs (e.g., Henry & Greenstein 1941). Due to the high

⁵ <https://archive.stsci.edu/prepds/alice/>

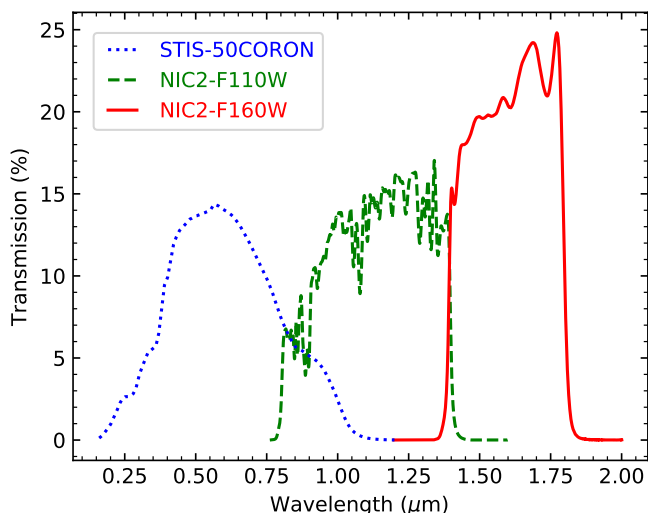


Fig. 1. Transmission of the STIS-50CORON, NIC2-F110W, and NIC2-F160W coronagraphic filters used to image debris disks in this study.

computational cost of NMF component calculation (Ren et al. 2018), we saved the components computed in data reduction for subsequent forward modeling. We present the reduced images in Fig. 3 and Fig. 4 for filters F110W and F160W, respectively.

As opposed to the classical PSF subtraction method used for the STIS observations where there are dedicated stable reference star images, the NMF algorithm used for NICMOS – which was shown to be able to better extract faint signals with higher quality than previous methods (e.g., Ren et al. 2018, 2021) – still introduces certain levels of overfit of disk signals. This is due to the diversity in stellar types, instrument observing conditions, and image stability in archival NICMOS observations, which makes the reference images not able to fully capture target PSFs for all observations in the near-infrared. To recover the surface brightness of a NICMOS disk, we did not adopt the scaling factor in Ren et al. (2018) that requires stable PSFs. Instead, we estimated the throughput of the algorithm by performing forward modeling to capture the PSF variation in the NICMOS archive. Specifically, we adopted the Millar-Blanchaer et al. (2015) code to create a disk model whose dust particles follow analytical SPFs in Henyey & Greenstein (1941), and modified them in our study.

To depict the spatial geometry of a debris disk, we used the Ren et al. (2021) modification of the Millar-Blanchaer et al. (2015) code: a combined power law in the disk mid-plane, and a vertical Gaussian dispersion, see Augereau et al. (1999). In cylindrical coordinates, the disk follows

$$\rho(r, z) \propto \left[\left(\frac{r}{r_c} \right)^{-2\alpha_{\text{in}}} + \left(\frac{r}{r_c} \right)^{-2\alpha_{\text{out}}} \right]^{-\frac{1}{2}} \exp \left[- \left(\frac{z}{hr} \right)^2 \right], \quad (1)$$

where r_c is the critical radius, $\alpha_{\text{in}} > 0$ and $\alpha_{\text{out}} < 0$ are the asymptotic power law indices when $r \ll r_c$ and $r \gg r_c$, respectively. Although the scale height parameter is $h = 0.04$ from a theoretical study by Thébaud (2009), we note that edge-on disks may deviate from this value and thus retrieve it in our disk modeling procedure. To account for the inner and outer clearing radii beyond which there is no dust particles, r_{in} and r_{out} , we only evaluate Equation (1) when $r_{\text{in}} < r < r_{\text{out}}$, and it equals 0 otherwise. To depict the SPF of the scatterers in a debris disk, we adopted a two-component Henyey–Greenstein function (e.g., Chen et al. 2020), since the original analytical phase function in Henyey

& Greenstein (1941) is monotonous, however that monotonicity is not always observed in actual debris disk observations (e.g., Stark et al. 2014; Chen et al. 2020).

For each target, we first generated a model disk image, then convolved it with the corresponding NICMOS point source PSF created by TinyTim (Krist et al. 2011)⁶ using the effective temperature of the star from Table 1. We subtracted the convolved disk from the observations to reperform NMF reduction using the originally calculated NMF components to reduce computational cost. In fact, for the debris disks in this study, we did not see major differences on re-computing the NMF components: this is likely due to the fact that the PSF wings are sufficiently brighter than debris disks in the data analyzed here, thus the latter do not contribute significantly to the selection of best-matching reference images. In comparison, when circumstellar disks are relatively brighter than PSF wings, we do indeed expect improvement of data reduction quality with NMF component re-computation (e.g., HD 100453 with VLT/SPHERE: Xie et al. 2023).

We distributed the calculation and forward modeling process using DebrisDiskFM (Ren et al. 2019) on a computer cluster, and explored the parameter space with emcee (Foreman-Mackey et al. 2013). The best-fit models minimize the residuals by maximizing the log-likelihood,

$$\ln \mathcal{L}(\Theta | X_{\text{obs}}) = -\frac{1}{2} \sum_{i=1}^N \left(\frac{X_{\text{obs},i} - X_{\text{model},i}}{\sigma_{\text{obs},i}} \right)^2 - \sum_{i=1}^N \ln \sigma_{\text{obs},i} - \frac{N}{2} \ln(2\pi), \quad (2)$$

where we have assumed that the pixels i follow independent normal distributions, with X_{obs} and X_{model} denoting the observation and model datasets, respectively. To quantify the uncertainty, we first obtained the algorithmic throughput of the best-fit model by comparing the model with the NMF reduction, then performed uncertainty measurement on the original individual NMF reductions with throughput correction.

2.3. Data for joint analysis

Given that the observed debris disks are of different inclinations, and that scatterers in debris disk systems redistribute incident light to different directions with varying intensity via SPFs (e.g., Stark et al. 2014; Milli et al. 2017), we measured the light with $\approx 90^\circ$ scattering angle to minimize such effects to enable a uniform comparison of different systems. We used the regions annotated in Appendix A.2 for measurements on the signal and background for both instruments. Specifically for NICMOS, by comparing our reduction of the original dataset with the best-fit convolved disk model, we can quantify the algorithmic throughput from the NMF post-processing procedure by dividing the NMF-reduced data with the best-fit model. We performed photometry on originally reduced data, subtracted flat halo backgrounds, and corrected the throughput measured from forward modeling. By doing so rather than performing measurements on the best-fit models, we expect to better capture the minor variations in observed disk signals.

We obtained the regions for birth ring photometry and halo background measurements as follows. Using the HD 181327 system as an example, we first identified the debris birth ring in

⁶ <http://tinytim.stsci.edu>

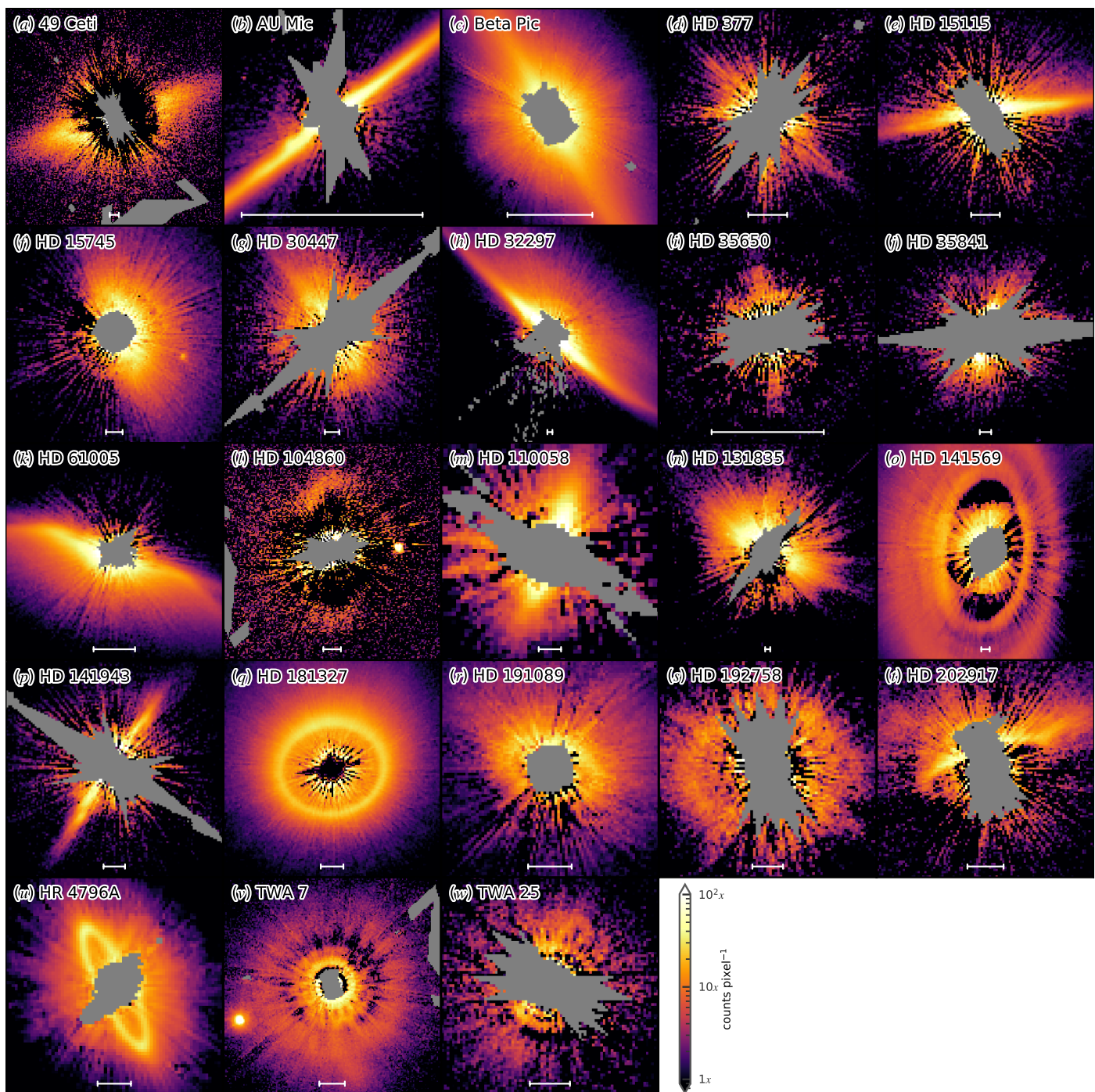


Fig. 2. Surface brightness distribution of the STIS disks. The color bars are in log scale with arbitrary units to adjust for difference in disk surface brightness across our debris disk gallery, and the scale bars are 50 au.

Figure A.1(q) using the ring parameters (e.g., semi-major axis, position angle, inclination) from Stark et al. (2014), then calculated for each pixel its scattering angle and associated angle uncertainty assuming an infinitely thin disk following Ren et al. (2019, Appendix A therein). To identify the pixels that host birth ring signals, if a pixel's 1σ range of scattering angles overlaps with the $[80^\circ, 100^\circ]$ interval, we categorize it as a birth ring pixel with $\approx 90^\circ$ scattering angle. To reduce certain contribution from the halo signals, we chose the pixels that are 1.5 times the distance of the birth ring from the star for HD 181327, and calculated their mean for a flat halo background removal in further steps. To further assess the variation of halo background at dif-

ferent locations surrounding HD 181327, we measured the halo background at distinct locations with varying region area (while avoiding known birth ring signals), and we observed no significant difference from the measured trends in Sect. 3.

For all debris systems, as a result, removing flat halo backgrounds induced minor deviation on the birth ring signals regardless of the location of the background pixels, since halos can be one or two orders of magnitude fainter than the birth rings (e.g., Schneider et al. 2014, 2018; Ren et al. 2019, 2021). In fact, the detected STIS halos in Fig. 2 and in NICMOS images are only evident in log scale display. Halo background removal in linear scale, as well as the variation of halo signals within the chosen

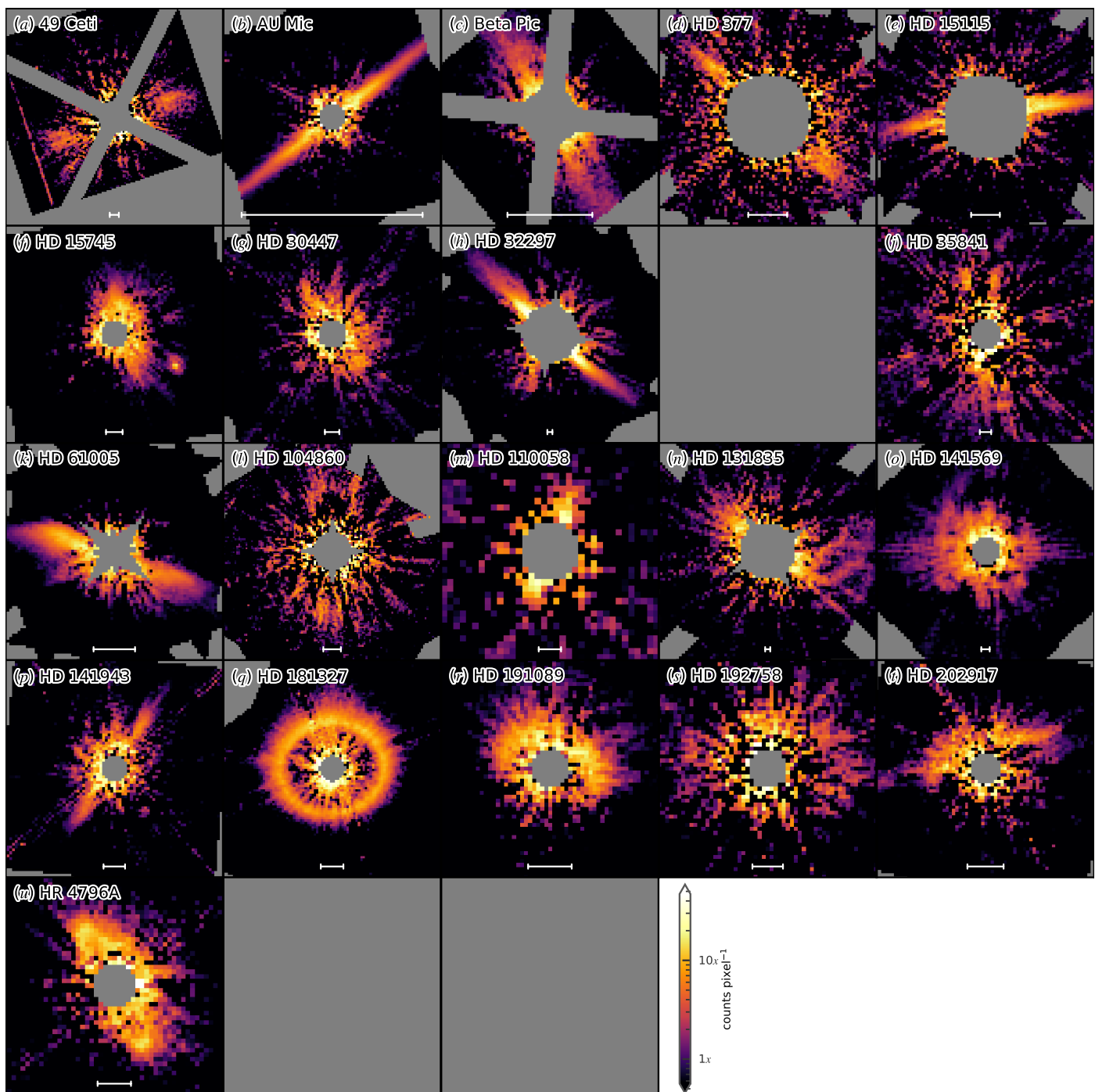


Fig. 3. Surface brightness distribution of the NICMOS disks using the F110W filter. The color bars are in log scale with arbitrary units, and the scale bars are 50 au.

regions, has minor influence ($<0.5\sigma$) on the extracted birth ring signals or the trend of birth ring color in Sect. 3.

We also note that for nearly edge-on systems (e.g., AU Mic, Beta Pic, HD 32297, HD 141943) where we performed measurements on the ansae of the debris disks, the measurements can actually probe a range of scattering angles that can deviate significantly from $\approx 90^\circ$. To explore possible measurement biases for these targets, as well as the impact of internal halo flat background at different regions for all targets, we varied the areas of regions for analysis for all systems by increasing or decreasing the signal and background extraction areas in Appendix A.2 by factors of up to 4 either individually or jointly, and we did not

observe statistically significant changes in our results or their interpretation in this study. We therefore adopt the regions identified in Appendix A.2 for further analysis on both birth ring color and flat halo background removal.

3. Analysis

We computed the STIS–NICMOS color of the disk images as follows. We first computed the reflectance in different filters for each system, then obtained the color for them.

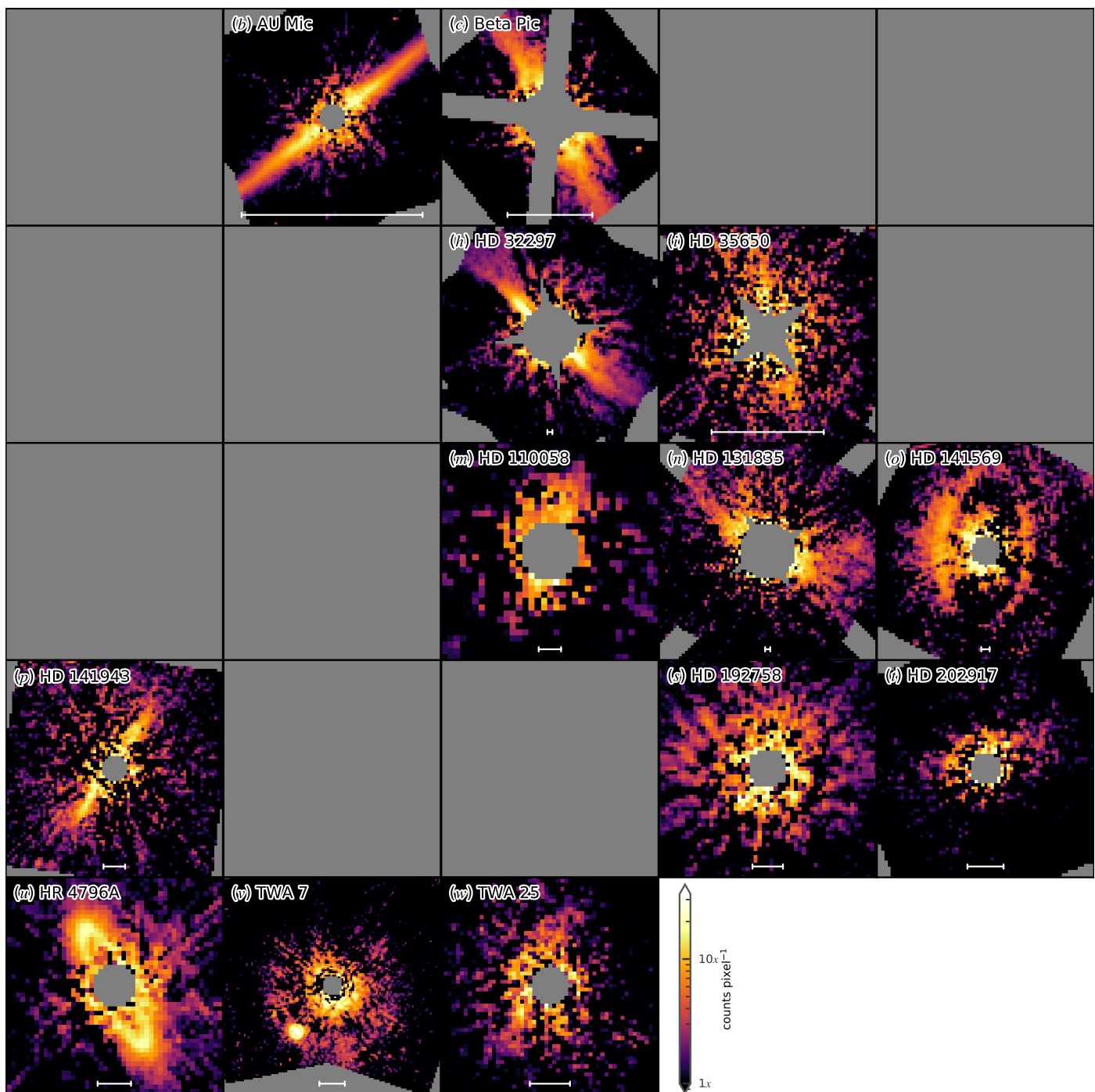


Fig. 4. Surface brightness distribution of the NICMOS disks using the F160W filter. The color bars are in log scale with arbitrary units, and the scale bars are 50 au.

3.1. Reflectance

We obtained the instrument response⁷ for the stars in units of Jy by calculating the unobstructed instrumental response to the Kurucz (1993) star models using *pysynphot* (STScI Development Team 2013), where the inputs are their effective temperature (T_{eff}), V-band magnitude, and surface gravity ($\log g$) in Table 1. For NICMOS F110W or NICMOS F160W, the parameter is ‘*nicmos, 2, f110w*’ or ‘*nicmos, 2, f160w*’, respectively.

⁷ The instrument response in this study refers to stellar flux density integrated in the instrument filters unless otherwise specified.

For STIS, ‘*stis,ccd,a2d4*’.⁸ We summarized the instrument response of the two coronagraphs in Table A.1.

For the pre- and post-NCS eras of NICMOS operation (i.e., Era 1 and Era 2, respectively; see, e.g., Schultz et al. 2003) where the sensitivities of the instrument are distinct, we adopted different PHOTFNU values to convert instrument counts to physical units of Jansky. For the two eras, the PHOTFNU parameter for F110W is 1.84724×10^{-6} and 2.03470×10^{-6} , respectively. For F160W, 1.21121×10^{-6} and 1.49585×10^{-6} . The *pysynphot* values correspond to Era 2 observations, for Era 1 observations

⁸ <https://pysynphot.readthedocs.io/en/latest/appendixb.html>

we thus first multiplied an instrument count rate by the PHOTFNU value in Era 2, then divided it by the PHOTFNU value in Era 1, to obtain the count rate in Era 1. For each image, we obtained the fraction of light reflected by the debris disk via dividing the calibrated image by the pysynphot rates for the star. We used these fraction images for color analysis.

3.2. Dust Color

To obtain the STIS–NICMOS color for a disk, we averaged 2×2 NICMOS pixels – 1 NICMOS pixel is 75.65 mas – into 1 bin, and 3×3 STIS pixels – 1 STIS pixel is 50.72 mas – into 1 bin, with each bin being a square with approximately 150 mas in length. We then divided the binned STIS image by the square of the ratio between the width of the STIS bin (152.16 mas) and that of the NICMOS bin (153.3 mas) to account for spatial scale difference, and converted the fraction values to magnitudes. To compare the reflectance in the two wavelengths for dust color, we subtracted the NICMOS magnitude from the STIS magnitude. In this way, a positive STIS–NICMOS value means the disk relatively scatters more light in NICMOS than in STIS, i.e., “red scatterer”, while taking into account of the effect in the intrinsic brightness of the host star at different wavelengths.

We computed the ansae color along the major axes of the disks, i.e., a scattering phase angle of $\approx 90^\circ$ between the incident light and the reflected light rays, to minimize the dependence of scattering intensity as a function of scattering phase angles (i.e., SPF, e.g., Hedman & Stark 2015). See Sect. 4.1 for a discussion on the contributions of signals from unbound particles (i.e., “flat halo background”), and the regions used for their removal. See Appendix A.2 for the regions used for color extraction and background removal.

We present the dust color at the ansae of the birth rings as a function of stellar luminosity, obtained from Stassun et al. (2018), in Fig. 5. Comparing STIS with NICMOS observations, we notice that the general color is blue, while it becomes more neutral when stellar luminosity increases. In comparison with existing debris disk color studies comparing STIS and NICMOS (e.g., Ren et al. 2019, 2021), the observed colors are consistent within 2σ despite different color extraction methods. Nevertheless, for HR 4796A in STIS and F110W, although Debes et al. (2008) and Rodigas et al. (2015) obtained red colors for the entire disk and the ansae, respectively, their results could have been compromised by the fact that certain signals were previously regarded as background before Schneider et al. (2018, Fig. 9 therein) and removed then. In fact, a blue ansae color measured for HR 4796A in this study is instead in agreement with the simulations from Thebault & Kral (2019), where the authors expected blue colors for debris birth rings for all A-type stars.

We observe that the F110W and F160W observations have a nearly neutral color, as well as a marginal trend with stellar luminosity in Fig. 5. A neutral color within the NICMOS wavelengths could rise from multiple aspects. First, the two NICMOS filters are adjacent to each other in wavelength in Fig. 1, which might not provide distinctive difference from dust properties. Second, the NICMOS data were observed under less stable instrument conditions than STIS: although the NMF data reduction and forward modeling steps had outperformed other classical or statistics-based methods in the results, the results are still dominated by instrument instability or incomplete reference image sampling in NICMOS observations. Third but not least, the sample size of debris disks observed in these filters are smaller than when they are compared with STIS observations. Due to these

aspects, we do not further discuss the trustworthiness of the color results within NICMOS wavelengths or their implications here.

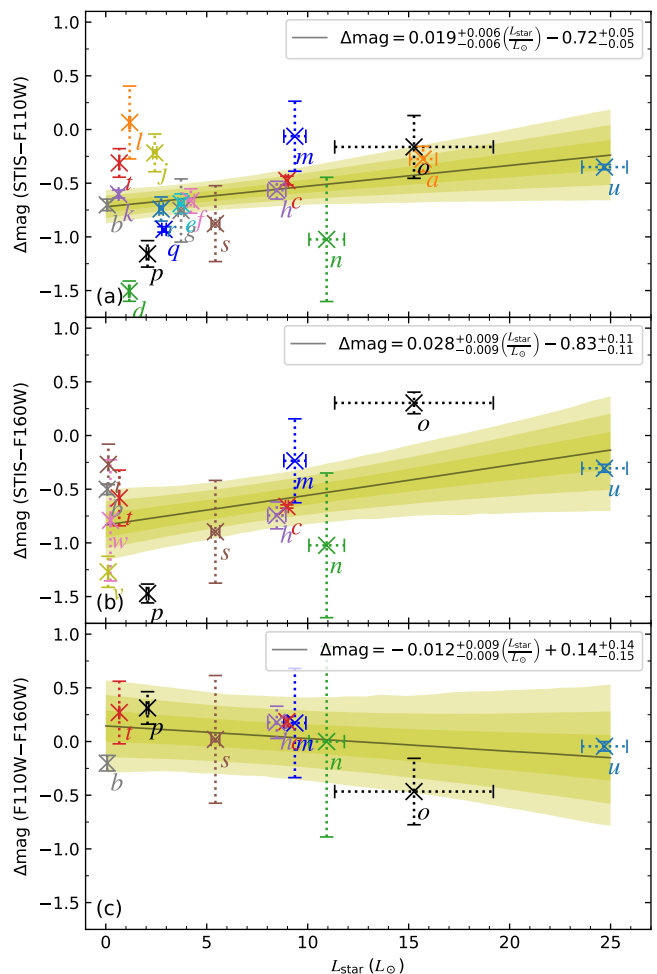


Fig. 5. Dust color at 80° – 100° scattering angle as a function of stellar luminosity. The letters next to the colorbars are the letter identifiers for the targets in Table 1. Panels (a) and (b) suggest that dust particles scatter light more efficiently at shorter wavelengths for less luminous stars. Although the trend in panel (c) does not agree with the other two, it is marginal and likely impacted by smaller sample size and data reduction artifacts. The shaded areas are 1σ , 2σ , and 3σ confidence bands from bootstrapping fit. See Table A.2 for the color values.

3.3. Color-albedo distribution: 90° -scattering albedo

In planetary science studies on Solar System minor objects (e.g., asteroids, comets, and zodiacal light), spectral gradient and albedo can show different properties of these objects. The normalized reflectivity gradient follows $S' = \frac{1}{S} \frac{dS}{d\lambda}$, where S is the reflectance at wavelength λ , and \bar{S} is the average reflectance (e.g., Yang & Ishiguro 2015). Under this convention, positive S' indicates that the scatterers are more efficient in scattering photons in longer wavelengths (defined as a “red” color in our study), see Figs. 1 and 6 in Yang & Ishiguro (2015) for a comparison between zodiacal light (red color in their Fig. 6) and different asteroids.

Noticing the fact that the measurement for an asteroid normally has a dominant scattering angle, while the resolved debris disks by *HST* have a range of scattering angles depending on their inclinations, we calculated a location-specific albedo for the debris disk samples in this study. Our definition of albedo is

performed on the resolved debris disk only for those regions that satisfy one criterion: within which the scattering angles of the dust particles are between 80° and 100° .

3.3.1. Albedo measurements

In an observed disk image in Fig. 2, the area of regions with $90^\circ \pm 10^\circ$ scattering angles can occupy a fraction $f_{[80^\circ, 100^\circ]} \in (0, 1]$ of the entire disk in the disk plane depending on the inclination of the disk: for a face-on disk, the entirety of the disk image has a 90° scattering angle; for an edge-on disk, only the on-sky ansae of the birth ring (rather than the entirety of the major axis) have $\sim 90^\circ$ scattering angle. To correct for this inclination-induced effect on the total scattered light at $\sim 90^\circ$ scattering angle, and recover all the scattered light that are not fully captured by the telescope due along our line of sight, our recovery of 90° -scattering albedo follows

$$\alpha_{[80^\circ, 100^\circ]} = \frac{\frac{F_{\text{disk}}/f_{[80^\circ, 100^\circ]}}{F_{\text{star}}}}{\frac{F_{\text{disk}}/f_{[80^\circ, 100^\circ]}}{F_{\text{star}}} + \frac{L_{\text{IR}}}{L_{\text{star}}}} \quad (3)$$

$$= \frac{\frac{F_{\text{disk}}}{F_{\text{star}}}}{\frac{F_{\text{disk}}}{F_{\text{star}}} + \frac{L_{\text{IR}}}{L_{\text{star}}} \times f_{[80^\circ, 100^\circ]}}, \quad (4)$$

where the disk flux F_{disk} is integrated in the observed disk region that satisfies the regional criteria. Indeed, by recovering the entire region of scattered light in Equation (3) using the partially observed data via $\frac{F_{\text{disk}}}{f_{[80^\circ, 100^\circ]}}$, it is equivalent to multiplying the infrared excess of the disk $\frac{L_{\text{IR}}}{L_{\text{star}}}$ by the fraction of the disk region in Equation (4).

Using the debris ring surface brightness values from STIS, we present the color–albedo measurements in Fig. 6. For the infrared excess values, we adopted the infrared excess data for HD 141569 from Mawet et al. (2017) and the rest from Cotten & Song (2016). We notice a likely L-shaped clustering of debris disk albedo and color for the samples. In comparison with Solar System objects, only B-type and some of C-type asteroids, both of which are carbonaceous and belong to C-group asteroids (Tholen 1989), have blue color while other commonly observed S-type (siliceous) and X-type (metal-rich) asteroids are reddish (e.g., Yang & Ishiguro 2015; Mählke et al. 2022).

3.3.2. Comparison with Solar System minor objects

In visible to near-infrared wavelengths, most of the icy Kuiper Belt objects are red (e.g., Tegler & Romanishin 2000; Jewitt & Luu 2001; Delsanti et al. 2006). Nevertheless, EL₆₁-group objects, which could have formed from a giant impact that removed ice mantles (e.g., Barkume et al. 2006; Brown et al. 2007), are slightly bluish (Merlin et al. 2007; Pinilla-Alonso et al. 2008). The EL₆₁ spectrum can be explained by a large amount of crystalline and amorphous water ice on the surface (Trujillo et al. 2007; Merlin et al. 2007). The albedos of Kuiper Belt objects, which are not necessarily measured at $\sim 90^\circ$ scattering angles as for debris disks in this study, have a large range from 0.01 to 0.8, with the majority of them below 0.2 (e.g., Fig. 3 of Stansberry et al. 2008). As for the Kuiper Belt dust, direct infrared observation is still not practical due to contamination of thermal emissions from the zodiacal cloud (Jewitt 2008; Brown 2012).

With an overarching caveat that the color–albedo studies on Solar System objects and on debris disks in Fig. 6 are on objects with distinct sizes (\sim km-sized objects and $\sim \mu$ m-sized par-

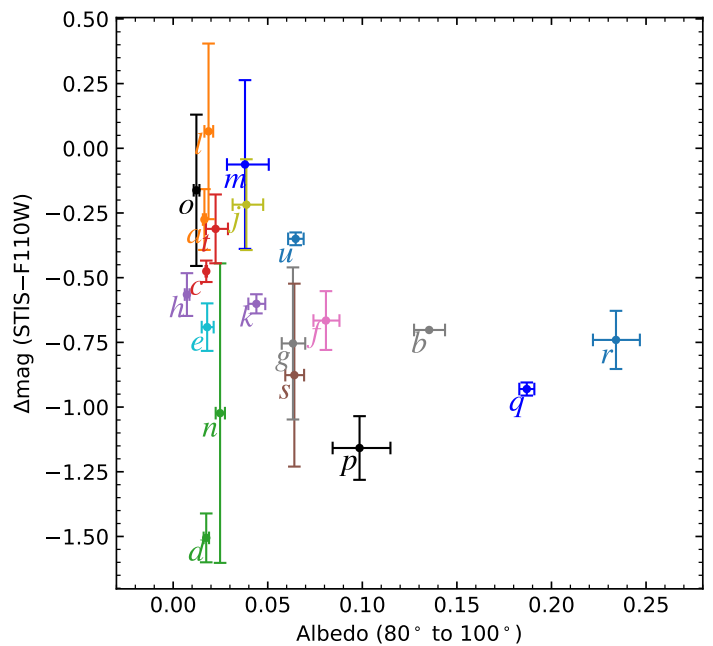


Fig. 6. Disk color and 90° -scattering albedo distribution defined in Equation (4). The likely L-shaped clustering of color-albedo distribution might resemble that of Solar System objects, which might indicate different formation history or composition of debris birth rings. See Table A.2 for the albedo values.

ticles, respectively), the color-albedo distribution of the debris disks here might qualitatively resemble some C-group asteroids and a very few Kuiper Belt objects (e.g., Yang & Ishiguro 2015, Fig. 1 therein). Nevertheless, given that the two albedos are calculated differently, although the debris disk albedos might resemble qualitatively most of C-type asteroids and Kuiper Belt objects, it does not suggest that the debris disk dust is made of materials that are identical to these Solar System objects.

In fact, in the young Solar System, dynamical processes can mix the minor objects within along the radial direction (DeMeo & Carry 2014). As a result, the current spatial locations of Solar System minor objects does not match their initial locations. Therefore, the colors of the planetary objects can change over time from mechanisms such as space weathering, in which high energy particles from the Sun and cosmic ray bombard these minor objects (Hapke 2001) with a timescale shorter than 1 Myr (Vernazza et al. 2009; DeMeo et al. 2023). Space weathering could cause both the reddening (Binzel et al. 2001) and the bluing (Moroz et al. 2004) of minor objects, depending on the size of the grains (Thompson et al. 2020) and the composition (e.g. C-type asteroids become bluer while S-type ones become redder: Nesvorný et al. 2005). The color change mechanisms for Solar System minor objects could further complicate the implications for the ensemble properties for the measurements of debris disks in this study.

Among Solar System minor objects, Q-type asteroids are considered to have fresh surfaces – which could retain pristine materials that might resemble debris disk dust – and are composed of ordinary chondrites. However, Hasegawa et al. (2019) showed that the color of minor object spectra could be the consequence of space weathering on grains larger than 100 microns. Therefore, given that the measured colors of Solar System objects are likely on dust that are $\sim 100 \mu\text{m}$ while the typical sizes of debris disk dust are $\sim 1 \mu\text{m}$ in scattered light here, there might not exist pristine materials on the surface of the current Solar

System objects, and thus a direct comparison of the colors between debris disks and Solar System objects is not feasible. Although we cannot directly match debris disks with Solar System minor objects, the likely L-shaped color-albedo distribution of the debris disks in Fig. 6 might indicate not only the difference in dust composition, but also different (levels of) activities such as space weathering in the observed debris systems.

3.3.3. Debris disk color-albedo clustering

The likely L-shaped clustering of debris disk albedo and color in Fig. 6, in comparison with that of Solar System objects albeit with a caveat in the different definition of albedos, indicates that the dust particles in different debris disk systems are formed differently and/or have different composition. Nevertheless, there exists an extra source of physically-motivated uncertainty for our measurements: the collisional simulation study by Thebault & Kral (2019) suggested that the halo outside the birth ring could contribute to $\sim 50\%$ of the flux up to $\sim 50 \mu\text{m}$.

The contribution from halo grains can impact infrared excess measurements (Thebault & Kral 2019), and consequently would bias the albedo values measured here: we assumed all the infrared excess – which is a combination from the birth ring and the halo – are from the debris ring in Equation (3). Given that the infrared excess signal from the birth ring alone is not easily separable in the Thebault & Kral (2019) study, we also investigated a possible lower limit of that signal. Specifically, to explore the influence of halo grains on SEDs, we adopted the infrared excess of cold belts from Chen et al. (2014) in which the authors performed two-belt fits to the SEDs. By applying the Chen et al. (2014) cold belt results to Equation (3), with a caveat the actual infrared excess could be lower (e.g., Thebault & Kral 2019), we only observed quantitative offsets for Fig. 6, and the different clusterings of color-albedo did not change qualitatively. However, noticing that two-belt SED fits still cannot intrinsically separate the contributions from the birth ring and the halo properly, the significant infrared excess contribution from halo grains in the Thebault & Kral (2019) study suggests that the actual albedo values should be different than those presented in Fig. 6.

4. Discussion

4.1. Blue color of debris disks

Comparing STIS and NICMOS observations of the debris disks in scattered light in $\sim 0.6 \mu\text{m}$ and in $\sim 1.1 \mu\text{m}$ or $\sim 1.6 \mu\text{m}$, we obtained a predominantly blue color at the ansae ($\approx 90^\circ$ scattering angle) of debris birth rings. The observed blue color can suggest the ubiquitous existence of the sub-micron-sized particles that scatter light more efficiently in shorter wavelengths than larger particles. Indeed, the theoretical simulation study in Thebault & Kral (2019) did show that even for A-type stars that were previously expected to blow sub-micron-sized dust out, high fractional luminosity disks ($\gtrsim 10^{-3}$) surrounding them can still harbor a sufficient number of these unbound dust (Fig. 2 therein) that are enough to make debris disks appear blue in scattered light (Fig. 13 therein).

While we have identified certain halo background areas that could aid in reducing the impact of unbound particles, the predominantly blue color of debris disk birth rings suggests that sub-micron-sized particles are widespread in all the systems studied here. What is more, the observed predominantly blue color suggests that a simple flat background removal adopted here has limited impacts on removing unbound dust contribu-

tion, since contributions from the SPFs of unbound particles are not negligible, especially when there exists an enough number of such particles as in Thebault & Kral (2019). Moreover, more importantly, there are other factors that could make the removal of a flat halo background less practical. First, Lee & Chiang (2016) simulations has shown that the existence of eccentric planet(s) can perturb the surface density distribution of halo particles. Second, the regions that we used to measure halo background have different stellocentric distances from that of the birth ring, requiring a distance-based illumination correction. Third but not least, the number density and surface density distributions of the unbound grains in the halo is not identical to that in the birth ring, calling for more investigations on the simulation results in or beyond Thebault & Kral (2019). Together with these limitations in removing the contribution from unbound particles on disk color measurement, a measurement of unbound particles in debris halo is not necessarily representative of the contribution of them at other locations including the birth ring. After all, the majority of debris disk birth rings indeed have blue colors, especially since sub-micron-sized particles – some of which are unbound when hosted by early-type stars – naturally reside in birth rings (e.g., Thebault & Kral 2019).

The blue debris ring color is more neutral for more luminous stars in Fig. 5. For the more luminous early-type stars, there could exist a small but sufficient number of sub-micron-sized particles that are unbound to make the debris rings blue (Thebault & Kral 2019). In comparison, the less luminous later-type stars can indeed retain sub-micron-sized particles (e.g., Arnold et al. 2019), and these bound particles could make debris rings appear blue. As a result, for debris disks orbiting stars with increasing stellar luminosity in Fig. 5, the sub-micron-sized particles within can turn from bound to unbound (i.e., from M-type to A-type stars), making the disks more neutral. Although it is not feasible to completely remove the color contribution from unbound particles in this study, the general trend of the color being more neutral for more luminous stars, if true, could be in line with the expectation that less sub-micron-sized particles are bound for earlier type stars, see Sect. 4.2 for a correlation between color and expected blowout size of dust particles.

Moving forward, to observationally better reveal the debris ring color for bound particles in debris systems (e.g., Fig. 13 of Thebault & Kral 2019, in which debris disks orbiting A-type stars turn from red to blue when unbound particles are taken into account), radiative transfer modelings of the SPFs for unbound particles are necessary to remove SPF effects at different scattering angles. Such modeling works would be achieved in principle by fitting the observed halo intensity as a function of scattering angle, then by extrapolating the brightness for the unbound particles at debris birth ring regions. However, these modelings could be challenging in terms of dust morphological model, size, composition, and computational feasibility (e.g., Tazaki & Tanaka 2018; Tazaki et al. 2019; Arnold et al. 2019), since they should be more realistic in resembling interplanetary dust particles (IDPs), which are produced from asteroid or comets from the inner main Asteroid Belt to the Kuiper Belt and they do have aggregate or fractal morphology (e.g., Bradley 2003). In addition, the Lee & Chiang (2016) simulations showed that the existence of hidden planetary perturber(s) on eccentric orbits can change the surface density distribution of particles in both the birth ring and the halo. We leave such an analysis on extracting debris birth ring colors only for bound particles for future studies.

4.2. Dust blowout size and disk color

A dust particle experiences the force balance between radiational pressure and gravity pull, and it becomes unbound when the former exceeds the latter on an orbital timescale. For a given stellar system, we can calculate the dust blowout size for non-porous dust using Equation (5) of Arnold et al. (2019) while assuming the average radiation-pressure efficiency over the stellar spectrum to be unity for compact spheres. Substituting the values for spherical amorphous olivine particles which have a mass density of 3.3 g cm^{-3} as in Chen et al. (2014), we obtain

$$a_{\text{BO}} = 0.35 \mu\text{m} \times \frac{L_{\text{star}}}{M_{\text{star}}}, \quad (5)$$

where L_{star} and M_{star} are in Solar units. See Column (10) of Table 1 for the corresponding dust blowout size. We note that we ignored dependences on dust properties such as composition and porosity (e.g., Arnold et al. 2019) to obtain a systematic view of the size information.

We fit the measured dust color with blow-out size using a linear relationship. There are positive correlations between the STIS–NICMOS colors and dust blow out size, or $\Delta\text{mag}_{\text{STIS-F110W}} = 0.12^{+0.05}_{-0.05} a_{\text{BO}} - 0.74^{+0.06}_{-0.06}$ and $\Delta\text{mag}_{\text{STIS-F160W}} = 0.17^{+0.07}_{-0.07} a_{\text{BO}} - 0.85^{+0.12}_{-0.12}$, respectively. The positive correlations indicate that larger dust scatters light relatively more efficiently at longer wavelengths, and thus make a debris system relatively redder.

Although there is a negative relationship between F110–F160W color and dust blow out size, or $\Delta\text{mag}_{\text{F110W-F160W}} = -0.07^{+0.07}_{-0.08} a_{\text{BO}} - 0.15^{+0.16}_{-0.15}$, the statistical significance is tangential. Given the facts that both F110W and F160W observations have undergone forward modeling procedure, and that only 10 out of the 23 systems have observations in both filters, such a negative relationship is likely impacted by data reduction artifact and small sample size. Nevertheless, we conclude that on the one hand, it is not fully valid to assume single composition or ignore porosity to calculate the actual blow out size for debris disk systems, and on the other hand, it is challenging to calculate dust color for adjacent filters when data reduction artifacts are non-negligible.

4.3. Disk infrared excess and disk color

We present the disk color dependence on fractional infrared excess ($L_{\text{IR}}/L_{\text{star}}$) in Fig. 7, with the infrared excess data from Sect. 3.3. We observe a trend that disks with higher fractional infrared excess are more neutral in color. Following theoretical studies in which infrared excess decreases over time (e.g., Wyatt et al. 2007; Löhne et al. 2008; Gáspár et al. 2013), this color trend might be correlated with disk evolutionary stage, yet such a trend has a caveat that the debris disk colors are already under steady state in theoretical simulation studies (e.g., Thebault & Kral 2019). What is more, more importantly, the fractional infrared excess is positively correlated with stellar luminosity in the samples in this study, making it probable that the former is not contributing to the color trend in Fig. 7.

To minimize the stellar luminosity contribution in the color dependence on fractional infrared excess, it is necessary to fit and remove stellar luminosity effects using Fig. 5. However, with the high dispersion of the data in stellar luminosity for the systems in this study, as well as the fact that the samples in this study are not from a uniform survey, a proper removal of stellar luminosity influences for Fig. 7 is beyond the scope of this study.

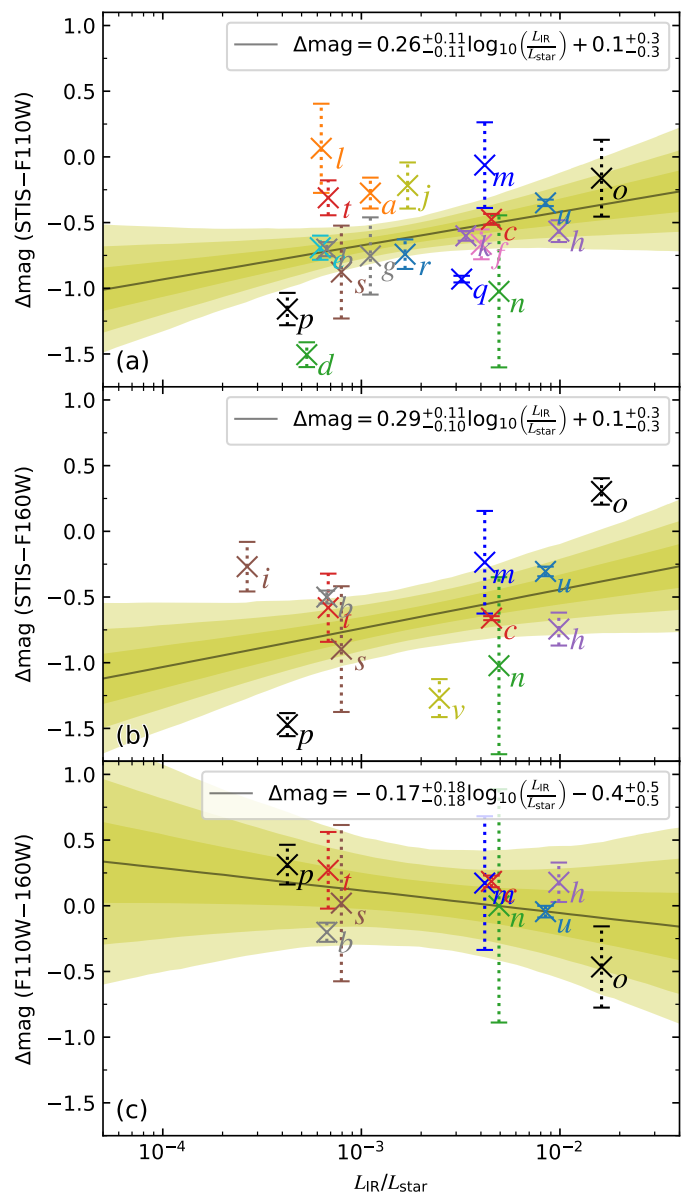


Fig. 7. Dust color as a function of fractional infrared excess. Panels (a), (b), (c) are for STIS–F110W, STIS–F160W, and F110W–F160W, respectively. With a caveat that infrared excess and stellar luminosity are positively correlated in Sect. 4.3, there might exist marginal trends of the STIS–NICMOS color being more neutral for disks with higher fractional infrared excess.

5. Conclusion

By extracting the resolved debris disks using the *Hubble Space Telescope* coronagraphs in visible and near-infrared light ($\sim 0.6 \mu\text{m}$, and $\sim 1.1 \mu\text{m}$ or $\sim 1.6 \mu\text{m}$) using classical reference differential imaging and forward modeling in the STIS and NICMOS coronagraphs, we obtained the reflectance of these debris disks in scattered light. We observe that the color of these disks is predominantly blue, which suggests that the dust particles in these systems scatter shorter-wavelength light more efficiently than longer-wavelength light.

In the albedo–color distribution of these systems, we notice the clustering of scatterers that could qualitatively resemble the clustering of Solar System objects, albeit with different definitions of albedos adopted. What is more, a qualitative resemblance does not indicate a compositional similarity. Were such

a clustering true for debris disks, it could indicate different formation history and compositions for these debris systems.

The dust particles in these systems scatter relatively more efficiently (rather than absolutely more efficiently) in longer wavelengths, as the luminosity of the host star increases. This correlates with the expectation that more luminous stars can blow out relatively larger dust particles, and thus shifting the dust color towards the relatively redder direction. Nevertheless, given that there could still harbor a large amount of sub-micron-sized unbound particles even in A-type stars (Thebault & Kral 2019), the measured blue color can rise from unbound particles in early-type stars as well as bound particles in late-type stars, which makes it challenging to separate these two kinds of contributions. A proper modeling and separation of scattered light contribution from unbound particles in the future is thus necessary to probe the birth ring color for bound particles in debris disks.

Accurate representation of the observed color and color-albedo distributions in debris disk systems requires the use of physically-motivated dust models. In comparison with existing attempts with Mie scatterers or a distribution of hollow spheres encountering difficulties in explaining observations (e.g., Milli et al. 2019; Ren et al. 2019; Chen et al. 2020; Arriaga et al. 2020), Olofsson et al. (2022) successfully reproduced the polarized light observations of HD 32297 with the Tazaki & Tanaka (2018) models. The usage of more sophisticated or realistic models (e.g., Arnold et al. 2019; Tazaki et al. 2019; Tobon Valencia et al. 2022) or lab measurements (e.g., Muñoz et al. 2021) to resemble the IDPs that are originated from the Asteroid Belt and the Kuiper Belt, are necessary to properly depict the observed color as well as albedo for circumstellar disks in future works.

Acknowledgements. We thank the anonymous referee for their comments that increased the clarity, depth, and width of this paper. We thank Xinyu Lu and Marco Delbo for helpful discussions. This work was funded by NASA through STScI Grant # *HST*-GO-15218.014-A for *HST* GO-15218 program (PI: É. Choquet). We are grateful for the productive discussions about dust scattering properties as part triggered by the EPOPEE (Etude des Poussières Planétaires Et Exoplanétaires) collaboration, supported by the French Planetology National Program (Programme National de Planétologie, PNP) of CNRS/INSU co-funded by CNES. We thank in particular Jean-Charles Augereau for helpful discussions about minimum grain sizes in debris disks and Jérémie Lasue for inspiring discussions about the diversity and properties of Solar System dust. E.C acknowledges funds from CNRS/PICS TACO-DESIRE program for supporting this research. This project has received funding from the European Research Council (ERC) under the European Union's Horizon 2020 research and innovation programme (PROTOPLANETS, grant agreement No. 101002188), and under the European Union's Horizon Europe research and innovation programme (ESCAPE, grant agreement No 101044152). Based on observations made with the NASA/ESA *Hubble Space Telescope*, obtained from the data archive at the Space Telescope Science Institute. STScI is operated by the Association of Universities for Research in Astronomy, Inc. under NASA contract NAS 5-26555. This research has made use of data reprocessed as part of the ALICE program, which was supported by NASA through grants *HST*-AR-12652 (PI: R. Soummer), *HST*-GO-11136 (PI: D. Golimowski), *HST*-GO-13855 (PI: É. Choquet), *HST*-GO-13331 (PI: L. Pueyo), and STScI Director's Discretionary Research funds, and was conducted at STScI which is operated by AURA under NASA contract NAS5-26555. This research has made use of the SIMBAD database (Wenger et al. 2000), operated at CDS, Strasbourg, France. This research has made use of the VizieR catalogue access tool, CDS, Strasbourg, France (DOI: 10.26093/cds/vizier). The original description of the VizieR service was published in A&AS 143, 23 (Ochsenbein et al. 2000). This research has made use of the SVO Filter Profile Service (<http://svo2.cab.inta-csic.es/theory/fps/>) supported from the Spanish MINECO through grant AYA2017-84089. The input images to ALICE processing are from the recalibrated NICMOS data products produced by the Legacy Archive project, "A Legacy Archive PSF Library And Circumstellar Environments (LAPLACE) Investigation," (*HST*-AR-11279, PI: G. Schneider). This work has made use of data from the European Space Agency (ESA) mission *Gaia* (<https://www.cosmos.esa.int/gaia>), processed by the *Gaia* Data Processing and Analysis Consortium (DPAC, <https://www.cosmos.esa.int/web/gaia/dpac/consortium>). Funding for the DPAC has been provided by national institutions, in particular the institutions participating in the *Gaia* Multilat-

eral Agreement. Part of the computations presented here were conducted in the Resnick High Performance Computing Center, a facility supported by Resnick Sustainability Institute at the California Institute of Technology.

References

- Anders, F., Khalatyan, A., Chiappini, C., et al. 2019, *A&A*, **628**, A94
 Apai, D., Schneider, G., Grady, C. A., et al. 2015, *ApJ*, **800**, 136
 Arnold, J. A., Weinberger, A. J., Videen, G., & Zubko, E. S. 2019, *AJ*, **157**, 157
 Arriaga, P., Fitzgerald, M. P., Duchêne, G., et al. 2020, *AJ*, **160**, 79
 Augereau, J. C., & Beust, H. 2006, *A&A*, **455**, 987
 Augereau, J. C., Lagrange, A. M., Mouillet, D., et al. 1999, *A&A*, **348**, 557
 Avenhaus, H., Quanz, S. P., Garufi, A., et al. 2018, *ApJ*, **863**, 44
 Barkume, K. M., Brown, M. E., & Schaller, E. L. 2006, *ApJ*, **640**, L87
 Beuzit, J.-L., Feldt, M., Dohlen, K., et al. 2008, *Proc. SPIE*, **7014**, 701418
 Binzel, R. P., Rivkin, A. S., Bus, S. J., et al. 2001, *M&PS*, **36**, 1167
 Bradley, J. P. 2003, *Treatise on Geochemistry*, **1**, 711
 Brown, M. E. 2012, *Annual Review of Earth and Planetary Sciences*, **40**, 467
 Brown, M. E., Barkume, K. M., Ragozzine, D., & Schaller, E. L. 2007, *Nature*, **446**, 294
 Cannon, A. J., & Pickering, E. C. 1993, *VizieR Online Data Catalog*, **III/135A**
 Chen, C., Mazoyer, J., Poteet, C. A., et al. 2020, *ApJ*, **898**, 55
 Chen, C. H., Mittal, T., Kuchner, M., et al. 2014, *ApJS*, **211**, 25
 Choquet, É., Pueyo, L., Hagan, J. B., et al. 2014, *Proc. SPIE*, **9143**, 914357
 Choquet, É., Milli, J., Wahhaj, Z., et al. 2017, *ApJ*, **834**, L12
 Choquet, É., Bryden, G., Perrin, M. D., et al. 2018, *ApJ*, **854**, 53
 Cotten, T. H., & Song, I. 2016, *ApJS*, **225**, 15
 David, T. J., & Hillenbrand, L. A. 2015, *ApJ*, **804**, 146
 Debes, J. H., Weinberger, A. J., & Schneider, G. 2008, *ApJ*, **673**, L191
 Delsanti, A., Peixinho, N., Boehnhardt, H., et al. 2006, *AJ*, **131**, 1851
 DeMeo, F. E., & Carry, B. 2014, *Nature*, **505**, 629
 DeMeo, F. E., Marsset, M., Polishook, D., et al. 2023, *Icarus*, **389**, 115264
 Dohnanyi, J. S. 1969, *JGR*, **74**, 2531
 Ducati, J. R. 2002, *VizieR Online Data Catalog*, **II/237**
 Duchêne, G., Rice, M., Hom, J., et al. 2020, *AJ*, **159**, 251
 Engler, N., Milli, J., Gratton, R., et al. 2022, *arXiv*, arXiv:2211.11767
 Ertel, S., Wolf, S., Metchev, S., et al. 2011, *A&A*, **533**, A132
 Esposito, T. M., Duchêne, G., Kalas, P., et al. 2018, *AJ*, **156**, 47
 Esposito, T. M., Kalas, P., Fitzgerald, M. P., et al. 2020, *AJ*, **160**, 24
 Fitzgerald, M. P., Kalas, P. G., Duchêne, G., et al. 2007, *ApJ*, **670**, 536
 Ford, H. C., Bartko, F., Bely, P. Y., et al. 1998, *Proc. SPIE*, **3356**, 234
 Foreman-Mackey, D., Hogg, D. W., Lang, D., & Goodman, J. 2013, *PASP*, **125**, 306
Gaia Collaboration, Brown, A. G. A., Vallenari, A., et al. 2018, *A&A*, **616**, A1
Gaia Collaboration, Vallenari, A., Brown, A. G. A., et al. 2022, *arXiv*, arXiv:2208.00211
 Gáspár, A., Rieke, G. H., & Balog, Z. 2013, *ApJ*, **768**, 25
 Golimowski, D. A., Ardila, D. R., Krist, J. E., et al. 2006, *AJ*, **131**, 3109
 Gray, R. O., Corbally, C. J., Garrison, R. F., et al. 2006, *AJ*, **132**, 161
 Gray, R. O., Riggs, Q. S., Koen, C., et al. 2017, *AJ*, **154**, 31
 Hagan, J. B., Choquet, É., Soummer, R., & Vigan, A. 2018, *AJ*, **155**, 179
 Hapke, B. 2001, *JGR*, **106**, 10039
 Harlan, E. A. 1974, *AJ*, **79**, 682
 Hasegawa, S., Hiroi, T., Ohtsuka, K., et al. 2019, *PASJ*, **71**, 103
 Heap, S. R., Lindler, D. J., Lanz, T. M., et al. 2000, *ApJ*, **539**, 435
 Hedman, M. M., & Stark, C. C. 2015, *ApJ*, **811**, 67
 Henyey, L. G., & Greenstein, J. L. 1941, *ApJ*, **93**, 70
 Herczeg, G. J., & Hillenbrand, L. A. 2014, *ApJ*, **786**, 97
 Høg, E., Fabricius, C., Makarov, V. V., et al. 2000, *A&A*, **355**, L27
 Houk, N. 1978, Michigan catalogue of two-dimensional spectral types for the HD stars (Ann Arbor, MI: Department of Astronomy, University of Michigan)
 —. 1982, Michigan Catalogue of Two-dimensional Spectral Types for the HD stars. Declinations -40° to -26°, Vol. 3 (Ann Arbor, MI: Department of Astronomy, University of Michigan)
 Houk, N., & Smith-Moore, M. 1988, Michigan Catalogue of Two-dimensional Spectral Types for the HD Stars. Declinations -26° to -12°, Vol. 4 (Ann Arbor, MI: Department of Astronomy, University of Michigan)
 Hughes, A. M., Duchêne, G., & Matthews, B. C. 2018, *ARA&A*, **56**, 541
 Jewitt, D. 2008, Saas-Fee Advanced Course 35: Trans-Neptunian Objects and Comets, **132**
 Jewitt, D. C., & Luu, J. X. 2001, *AJ*, **122**, 2099
 Kahraman Aliçavuş, F., Niemczura, E., De Cat, P., et al. 2016, *MNRAS*, **458**, 2307
 Kalas, P. 2005, *ApJ*, **635**, L169
 Kalas, P., Fitzgerald, M. P., & Graham, J. R. 2007, *ApJ*, **661**, L85
 Keenan, P. C., & McNeil, R. C. 1989, *ApJS*, **71**, 245
 Kiraga, M. 2012, *Acta Astron.*, **62**, 67
 Konishi, M., Grady, C. A., Schneider, G., et al. 2016, *ApJ*, **818**, L23

- Krist, J. E., Hook, R. N., & Stoehr, F. 2011, *Proc. SPIE*, 8127, 81270J
- Krist, J. E., Stapelfeldt, K. R., Bryden, G., & Plavchan, P. 2012, *AJ*, 144, 45
- Krist, J. E., Stapelfeldt, K. R., Bryden, G., et al. 2010, *AJ*, 140, 1051
- Krivov, A. V., Löhne, T., & Sremčević, M. 2006, *A&A*, 455, 509
- Kurucz, R. 1993, ATLAS9 Stellar Atmosphere Programs and 2 km/s grid. Kurucz CD-ROM No. 13. Cambridge, 13
- Lagrange, A.-M., Chauvin, G., Fusco, T., et al. 2003, *Proc. SPIE*, 4841, 860
- Laws, A. S. E., Harries, T. J., Setterholm, B. R., et al. 2020, *ApJ*, 888, 7
- Lee, E. J., & Chiang, E. 2016, *ApJ*, 827, 125
- Lenzen, R., Hartung, M., Brandner, W., et al. 2003, *Proc. SPIE*, 4841, 944
- Löhne, T., Krivov, A. V., & Rodmann, J. 2008, *ApJ*, 673, 1123
- Macintosh, B. A., Graham, J. R., Palmer, D. W., et al. 2008, *Proc. SPIE*, 7015, 701518
- Mahlke, M., Carry, B., & Mattei, P. A. 2022, *A&A*, 665, A26
- Mawet, D., Choquet, É., Absil, O., et al. 2017, *AJ*, 153, 44
- Merlin, F., Guilbert, A., Dumas, C., et al. 2007, *A&A*, 466, 1185
- Millar-Blanchaer, M. A., Graham, J. R., Pueyo, L., et al. 2015, *ApJ*, 811, 18
- Milli, J., Mawet, D., Pinte, C., et al. 2015, *A&A*, 577, A57
- Milli, J., Vigan, A., Mouillet, D., et al. 2017, *A&A*, 599, A108
- Milli, J., Engler, N., Schmid, H. M., et al. 2019, *A&A*, 626, A54
- Moroz, L., Baratta, G., Strazzulla, G., et al. 2004, *Icarus*, 170, 214
- Mouillet, D., Lagrange, A. M., Augereau, J. C., & Ménard, F. 2001, *A&A*, 372, L61
- Muñoz, O., Frattin, E., Jardiel, T., et al. 2021, *ApJS*, 256, 17
- Nesvorný, D., Jedicke, R., Whiteley, R. J., & Ivezić, Ž. 2005, *Icarus*, 173, 132
- Ochsenbein, F., Bauer, P., & Marcout, J. 2000, *A&AS*, 143, 23
- Olofsson, J., Milli, J., Bayo, A., et al. 2020, *A&A*, 640, A12
- Olofsson, J., Thébault, P., Kennedy, G. M., & Bayo, A. 2022, *A&A*, 664, A122
- Pan, M., & Schlichting, H. E. 2012, *ApJ*, 747, 113
- Pawellek, N., & Krivov, A. V. 2015, *MNRAS*, 454, 3207
- Pawellek, N., Krivov, A. V., Marshall, J. P., et al. 2014, *ApJ*, 792, 65
- Pawellek, N., Moór, A., Milli, J., et al. 2019, *MNRAS*, 488, 3507
- Pinilla-Alonso, N., Licandro, J., & Lorenzi, V. 2008, *A&A*, 489, 455
- Ramberg, E. 1993, *Proc. SPIE*, 1945, 383
- Ren, B., Pueyo, L., Chen, C., et al. 2020, *ApJ*, 892, 74
- Ren, B., Pueyo, L., Zhu, G. B., et al. 2018, *ApJ*, 852, 104
- Ren, B., Choquet, É., Perrin, M. D., et al. 2019, *ApJ*, 882, 64
- . 2021, *ApJ*, 914, 95
- Riley, A., et al. 2018, STIS Instrument Handbook, Version 17.0 (Baltimore, MD: STScI)
- Rodigas, T. J., Debes, J. H., Hinz, P. M., et al. 2014, *ApJ*, 783, 21
- Rodigas, T. J., Stark, C. C., Weinberger, A., et al. 2015, *ApJ*, 798, 96
- Rodrigo, C., & Solano, E. 2020, 182
- Rodrigo, C., Solano, E., & Bayo, A. 2012, SVO Filter Profile Service Version 1.0, IVOA Working Draft 15 October 2012, IVOA Working Draft 15 October 2012
- Schneider, G., Gaspar, A., Debes, J., et al. 2017, Enabling Narrow(est) IWA Coronagraphy with STIS BAR5 and BAR10 Occulters, Tech. rep., 3
- Schneider, G., Grady, C. A., Hines, D. C., et al. 2014, *AJ*, 148, 59
- Schneider, G., Grady, C. A., Stark, C. C., et al. 2016, *AJ*, 152, 64
- Schneider, G., Debes, J. H., Grady, C. A., et al. 2018, *AJ*, 155, 77
- Schultz, A. B., Sosey, M., Mazzuca, L. M., et al. 2003, *Proc. SPIE*, 4850, 858
- Soummer, R., Perrin, M. D., Pueyo, L., et al. 2014, *ApJ*, 786, L23
- Stansberry, J., Grundy, W., Brown, M., et al. 2008, Physical Properties of Kuiper Belt and Centaur Objects: Constraints from the Spitzer Space Telescope, ed. M. A. Barucci, H. Boehnhardt, D. P. Cruikshank, A. Morbidelli, & R. Dotson, 161
- Stark, C. C., Schneider, G., Weinberger, A. J., et al. 2014, *ApJ*, 789, 58
- Stassun, K. G., Oelkers, R. J., Pepper, J., et al. 2018, *AJ*, 156, 102
- Strubbe, L. E., & Chiang, E. I. 2006, *ApJ*, 648, 652
- STScI Development Team. 2013, pysynphot: Synthetic photometry software package, *ASCL*, 1303.023
- Tazaki, R., & Tanaka, H. 2018, *ApJ*, 860, 79
- Tazaki, R., Tanaka, H., Muto, T., et al. 2019, *MNRAS*, 485, 4951
- Tegler, S. C., & Romanishin, W. 2000, *Nature*, 407, 979
- Thébaud, P. 2009, *A&A*, 505, 1269
- Thebaud, P., & Kral, Q. 2019, *A&A*, 626, A24
- Tholen, D. J. 1989, Asteroids II, 1139
- Thompson, M. S., Morris, R. V., Clemett, S. J., et al. 2020, *Icarus*, 346, 113775
- Thompson, R. 1992, *Space Sci. Rev.*, 61, 69
- Tobon Valencia, V., Geffrin, J.-M., Ménard, F., et al. 2022, *A&A*, 666, A68
- Torres, C. A. O., Quast, G. R., da Silva, L., et al. 2006, *A&A*, 460, 695
- Trujillo, C. A., Brown, M. E., Barkume, K. M., et al. 2007, *ApJ*, 655, 1172
- Vernazza, P., Binzel, R. P., Rossi, A., et al. 2009, *Nature*, 458, 993
- Viana, A., Wiklund, T., et al. 2009, NICMOS Instrument Handbook, Version 11.0 (Baltimore, MD: STScI)
- Wenger, M., Ochsenbein, F., Egret, D., et al. 2000, *A&AS*, 143, 9
- Woodgate, B. E., Kimble, R. A., Bowers, C. W., et al. 1998, *PASP*, 110, 1183
- Wyatt, M. C. 2008, *ARA&A*, 46, 339
- Wyatt, M. C., Smith, R., Su, K. Y. L., et al. 2007, *ApJ*, 663, 365
- Xie, C., Ren, B., Dong, R., et al. 2023, in preparation
- Yang, H., & Ishiguro, M. 2015, *ApJ*, 813, 87
- Zacharias, N., Finch, C. T., Girard, T. M., et al. 2012, VizieR Online Data Catalog, I/322A

Appendix A: Supplementary Materials

A.1. Exposure information of targets

We summarize the exposure time information for the targets in Table A.1.

A.2. Color extraction locations

We display the regions used to extract color information for the dust in Fig. A.1.

A.3. Color and albedo values

We present the extracted color and albedo values in Table A.2.

Table A.1. Exposure Time and Instrument Response for Debris Disk Hosts

Instrument		F110W	F160W	STIS	F110W	F160W	STIS
id (1)	Target (2)	Exposure Time (s)			Instrument Response (Jy)		
		(3)	(4)	(5)	(6)	(7)	(8)
<i>a</i>	49 Ceti	2335.57	...	1918.8	11.0	...	16.3
<i>b</i>	AU Mic	2687.53	2687.53	13050	5.45	7.65	1.48
<i>c</i>	Beta Pic	127.78 ^a	47.92 ^a	2575.8	85.7	60.8	83.3
<i>d</i>	HD 377	4319.38	...	4596.6	4.08	...	2.76
<i>e</i>	HD 15115	4607.27	...	11484.8	6.21	...	5.59
<i>f</i>	HD 15745	1407.76	...	17730	3.26	...	2.96
<i>g</i>	HD 30447	1343.76	...	4320	2.41	...	2.11
<i>h</i>	HD 32297	1343.76	1343.76	13228.2	1.29	0.832	1.58
<i>i</i>	HD 35650	...	1503.57	6055.8	...	4.11	0.939
<i>j</i>	HD 35841	1343.76	...	4350	1.05	...	0.816
<i>k</i>	HD 61005	4607.34	...	13284	2.65	...	1.57
<i>l</i>	HD 104860	5183.26	...	6360	2.97	...	2.05
<i>m</i>	HD 110058	2303.6	2303.6	4708.8	1.49	0.956	1.84
<i>n</i>	HD 131835	2303.6	2303.6	4672.5	1.57	0.981	2.04
<i>o</i>	HD 141569	1215.76 ^a	863.5 ^a	16005.6	2.98	1.83	4.03
<i>p</i>	HD 141943	4607.34	1535.56	4479.6	3.09	2.74	1.95
<i>q</i>	HD 181327	1535.69	...	12812	5.58	...	4.51
<i>r</i>	HD 191089	4607.34	...	7847.6	4.89	...	3.97
<i>s</i>	HD 192758	3455.41	3455.41	4078.8	4.49	3.14	4.48
<i>t</i>	HD 202917	3519.51	1407.74 ^a	14034	1.75	1.62	1.04
<i>u</i>	HR 4796A	1951.65 ^a	2367.57 ^a	9525.6	8.72	5.05	14.2
<i>v</i>	TWA 7	...	1215.76 ^a	6718.8	...	0.953	0.177
<i>w</i>	TWA 25	...	1503.57	14508	...	0.755	0.141

Notes: Column (1): letter identifiers of targets. Column (2): target name. Columns (3), (4), and (5): exposure time using F110W, F160W, and STIS, respectively. Columns (6), (7), and (8): pysynphot instrumental response for the unocculted stars using F110W, F160W, and STIS, respectively, with 3 significant digits.
^aObserved in NICMOS Era 1.

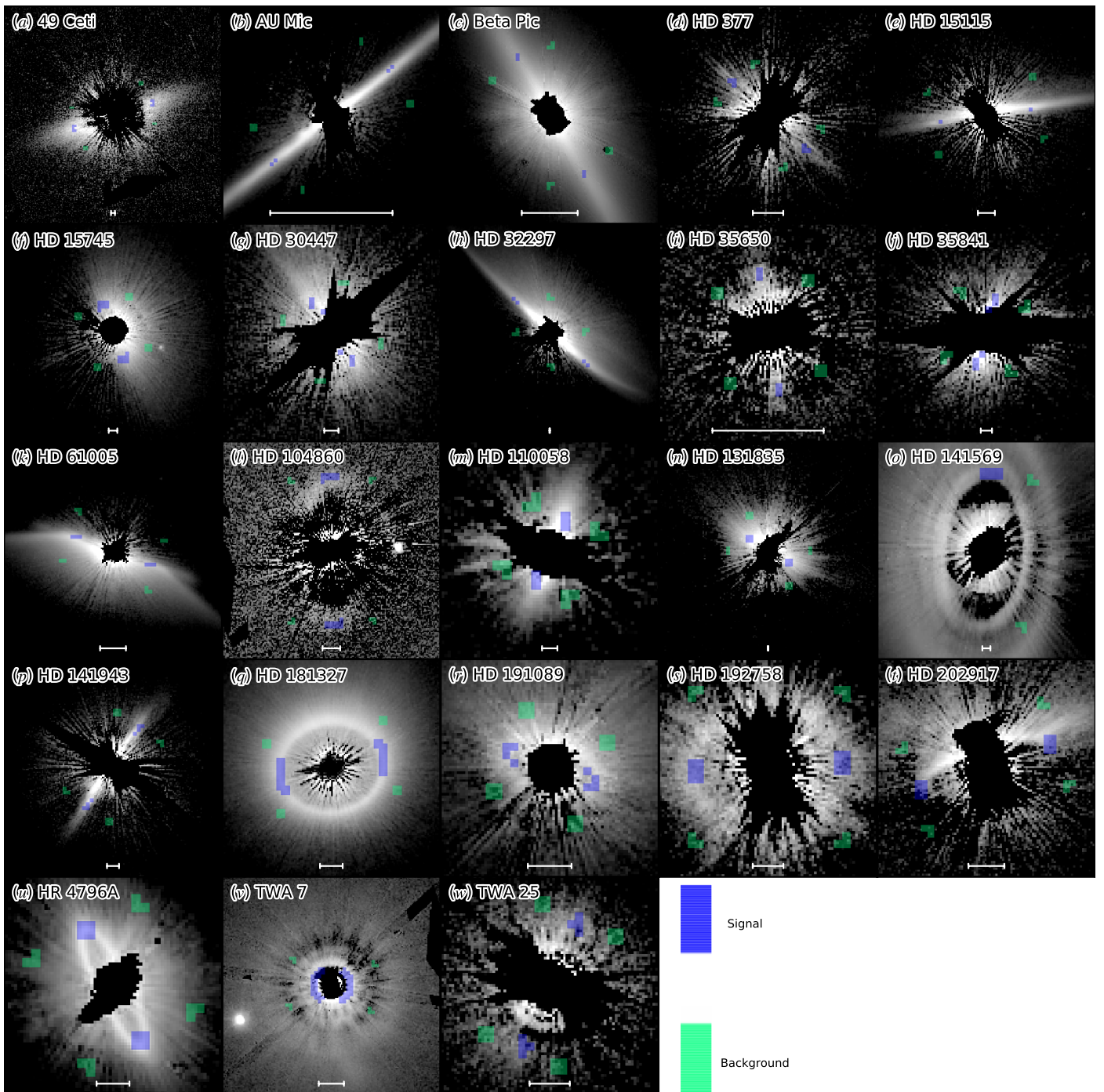


Fig. A.1. Regions used for dust color extraction (at 80° – 100° scattering angle) and background removal overlaid onto STIS images. The surface brightness distributions of the disks are presented in log scale. When we changed the area of either or both regions by up to a factor of 4, the observed trends in both color and albedo did not have significant variation.

Table A.2. Color and albedo information measured in this study

id (1)	Target (2)	STIS-F110W (3)	STIS-F160W (4)	F110W-F160W (5)	albedo(STIS-F110W) (6)
<i>a</i>	49 Ceti	$-0.28^{+0.12}_{-0.12}$	$0.0165^{+0.0009}_{-0.0008}$
<i>b</i>	AU Mic	$-0.7^{+0.05}_{-0.05}$	$-0.5^{+0.05}_{-0.05}$	$-0.2^{+0.07}_{-0.07}$	$0.135^{+0.008}_{-0.008}$
<i>c</i>	Beta Pic	$-0.48^{+0.04}_{-0.04}$	$-0.661^{+0.015}_{-0.015}$	$0.19^{+0.04}_{-0.04}$	$0.0175^{+0.0004}_{-0.0004}$
<i>d</i>	HD 377	$-1.51^{+0.09}_{-0.09}$	$0.0175^{+0.0015}_{-0.0014}$
<i>e</i>	HD 15115	$-0.69^{+0.09}_{-0.09}$	$0.018^{+0.003}_{-0.003}$
<i>f</i>	HD 15745	$-0.67^{+0.11}_{-0.11}$	$0.081^{+0.007}_{-0.007}$
<i>g</i>	HD 30447	$-0.8^{+0.3}_{-0.3}$	$0.063^{+0.006}_{-0.006}$
<i>h</i>	HD 32297	$-0.57^{+0.08}_{-0.08}$	$-0.74^{+0.13}_{-0.13}$	$0.18^{+0.15}_{-0.15}$	$0.0073^{+0.0013}_{-0.0011}$
<i>i</i>	HD 35650	...	$-0.27^{+0.13}_{-0.19}$...	$0.052^{+0.005}_{-0.004}$
<i>j</i>	HD 35841	$-0.22^{+0.18}_{-0.18}$	$0.039^{+0.009}_{-0.007}$
<i>k</i>	HD 61005	$-0.6^{+0.04}_{-0.04}$	$0.044^{+0.005}_{-0.004}$
<i>l</i>	HD 104860	$0.1^{+0.3}_{-0.3}$	$0.019^{+0.002}_{-0.002}$
<i>m</i>	HD 110058	$-0.1^{+0.3}_{-0.3}$	$-0.2^{+0.4}_{-0.4}$	$0.2^{+0.5}_{-0.5}$	$0.038^{+0.013}_{-0.010}$
<i>n</i>	HD 131835	$-1.0^{+0.6}_{-0.6}$	$-1.0^{+0.7}_{-0.7}$	$-0.0^{+0.9}_{-0.9}$	$0.025^{+0.003}_{-0.002}$
<i>o</i>	HD 141569	$-0.2^{+0.3}_{-0.3}$	$0.30^{+0.10}_{-0.10}$	$-0.5^{+0.3}_{-0.3}$	$0.0123^{+0.0016}_{-0.0014}$
<i>p</i>	HD 141943	$-1.16^{+0.12}_{-0.12}$	$-1.47^{+0.09}_{-0.09}$	$0.31^{+0.15}_{-0.15}$	$0.099^{+0.016}_{-0.014}$
<i>q</i>	HD 181327	$-0.93^{+0.03}_{-0.03}$	$0.187^{+0.004}_{-0.004}$
<i>r</i>	HD 191089	$-0.74^{+0.11}_{-0.11}$	$0.234^{+0.013}_{-0.012}$
<i>s</i>	HD 192758	$-0.9^{+0.4}_{-0.4}$	$-0.9^{+0.5}_{-0.5}$	$0.0^{+0.6}_{-0.6}$	$0.064^{+0.005}_{-0.005}$
<i>t</i>	HD 202917	$-0.31^{+0.13}_{-0.13}$	$-0.6^{+0.3}_{-0.3}$	$0.3^{+0.3}_{-0.3}$	$0.022^{+0.007}_{-0.005}$
<i>u</i>	HR 4796A	$-0.35^{+0.02}_{-0.02}$	$-0.31^{+0.04}_{-0.04}$	$-0.04^{+0.04}_{-0.04}$	$0.065^{+0.004}_{-0.004}$
<i>v</i>	TWA 7	...	$-1.27^{+0.14}_{-0.14}$...	$0.57^{+0.02}_{-0.02}$
<i>w</i>	TWA 25	...	$-0.8^{+0.6}_{-0.6}$

Notes: Column (1): letter identifiers of the targets in this paper. Column (2): target name. Column (3): STIS - F110W color. Column (4): STIS - F160W color. Column (5): F110W - F160W color. Column (6): 90°-scattering albedo for STIS-F110W color.